AGU PUBLICATIONS

Geophysical Research Letters

RESEARCH LETTER
10.1002/2015GL065072

Key Points:
- Maximum possible magnitude during fluid injection depends on fault orientation
- Along critically stressed faults the rupture-front may propagate beyond the pressure front
- Fault orientations and stress field can be included in induced seismic hazard analysis

Supporting Information:
- Supporting Information S1

Correspondence to:
V. S. Gischig,
gischig@erdw.ethz.ch

Citation:
Gischig, V. S. (2015), Rupture propagation behavior and the largest possible earthquake induced by fluid injection into deep reservoirs, *Geophys. Res. Lett.*, *42*, 7420–7428, doi:10.1002/2015GL065072.

Received 24 JUN 2015
Accepted 24 AUG 2015
Accepted article online 25 AUG 2015
Published online 21 SEP 2015

Rupture propagation behavior and the largest possible earthquake induced by fluid injection into deep reservoirs

Valentin S. Gischig[1]

[1]Swiss Competence Center for Energy Research (SCCER-SoE), ETH Zurich, Zurich, Switzerland

Abstract Earthquakes caused by fluid injection into deep underground reservoirs constitute an increasingly recognized risk to populations and infrastructure. Quantitative assessment of induced seismic hazard, however, requires estimating the maximum possible magnitude earthquake that may be induced during fluid injection. Here I seek constraints on an upper limit for the largest possible earthquake using source-physics simulations that consider rate-and-state friction and hydromechanical interaction along a straight homogeneous fault. Depending on the orientation of the pressurized fault in the ambient stress field, different rupture behaviors can occur: (1) uncontrolled rupture-front propagation beyond the pressure front or (2) rupture-front propagation arresting at the pressure front. In the first case, fault properties determine the earthquake magnitude, and the upper magnitude limit may be similar to natural earthquakes. In the second case, the maximum magnitude can be controlled by carefully designing and monitoring injection and thus restricting the pressurized fault area.

1. Introduction

The number of anthropogenically induced earthquakes caused by deep underground operations, such as hydraulic stimulation, has grown at an exceptional rate as subsurface resources (geothermal energy, shale gas, etc.) are increasingly exploited [*Ellsworth*, 2013]. Many of these earthquakes have been of moderate magnitude and felt by local inhabitants and in several cases even caused damage: e.g., M_w3.0 during reservoir stimulation in Basel, Switzerland [*Häring et al.*, 2008]; M_w5.7 during waste water injection in Oklahoma, USA [*Keranen et al.*, 2013]. Therefore, the discussion of what is the maximum magnitude earthquake potentially created by fluid injection has become increasingly pertinent [*Gischig and Wiemer*, 2013; *McGarr*, 1976, 2014]. This worst case event is one of the critical parameters (besides, e.g., Gutenberg-Richter *b* value and ground motion prediction equations) for quantitative assessment of induced seismic hazard and risk, which is in turn an essential requirement for project development and permitting of enhanced geothermal projects in densely populated regions (Figure 1) [*Giardini*, 2009; *Mignan et al.*, 2015]. In this context, the maximum possible magnitude (M_{max} hereafter) corresponds to the earthquake that is rare but still possible based on geological and geophysical considerations [*Wiemer et al.*, 2009].

In tectonic seismic hazard studies, M_{max} is estimated from the largest earthquake in similar tectonic regimes [*Petersen et al.*, 2008], the largest fault within the considered tectonic region that may be reactivated, based on historic earthquakes or paleoseismological evidence [*Wiemer et al.*, 2009]. It is the magnitude at which the Gutenberg-Richter relation (the power law distribution typically representing the frequency of occurrence versus earthquake magnitudes) is truncated at high magnitudes (Figure 1b) [*Mena et al.*, 2013; *Wiemer et al.*, 2009]. In an induced seismicity context, it must not be confused with the actual maximum magnitude recorded during or after fluid injection, as M_{max} may substantially exceed this value. Despite its low probability of occurrence, M_{max} has an impact on hazard and risk estimates from induced seismicity [*Bachmann et al.*, 2011; *Mena et al.*, 2013; *Mignan et al.*, 2015] (Figure 1c). (It is mentionable that although hazard estimates are sensitive to M_{max}, the ground motion prediction equations usually have a stronger impact [*Atkinson et al.*, 2015; *Mignan et al.*, 2015].) The optimistic view on M_{max} is that it can be readily estimated from the volume of injected fluid or from the stimulated reservoir size and hence is relatively small. This is based on the empirical observation that either the upper limit of maximum seismic moment released during injection is proportional to the injected fluid volume [*Bourne et al.*, 2015; *McGarr*, 1976, 2014] or that the maximum source area is contained within the pressurized rock volume [*Baisch et al.*, 2009]. The conservative view on M_{max} is based on the notion that a large, critically stressed fault may happen to cross the stimulated rock

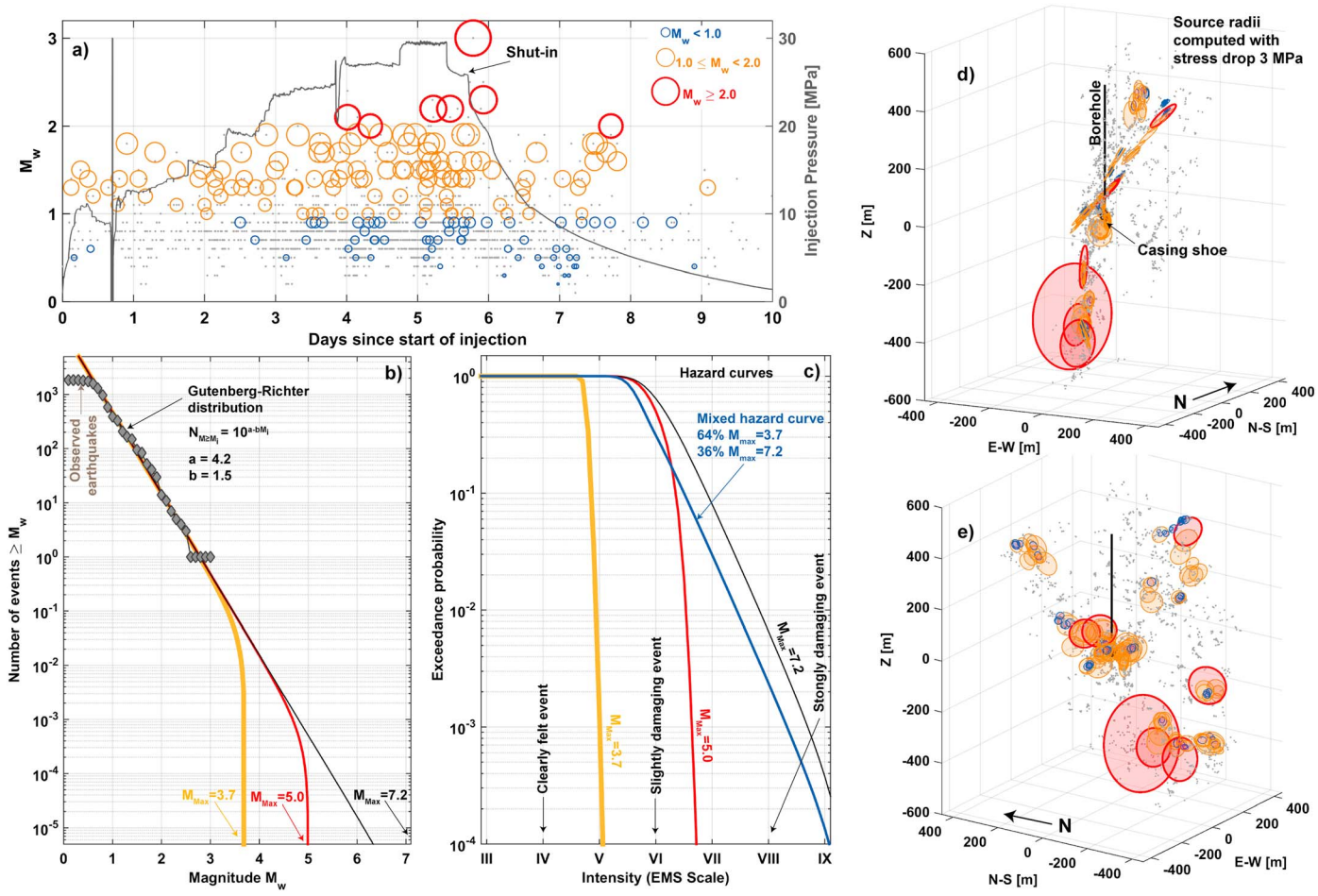

Figure 1. Seismicity during reservoir stimulation at the Basel EGS project (injection start: 22:00, 2 December 2006). (a) Earthquake magnitudes and wellhead pressure versus time. Grey dots are from the relocated event catalogue [*Kraft and Deichmann*, 2014]. For a subset of these (colored), cluster analysis was possible [*Deichmann et al.*, 2014]. (b) Frequency-magnitude distribution of the grey events in Figure 1a and best fit Gutenberg-Richter distribution truncated at different M_{max} values. (c) Hazard curves: probability of exceeding a certain shaking intensity during the 10 days of seismicity shown in Figure 1a [*Bachmann et al.*, 2011; *Mena et al.*, 2013]. The hazard curves were computed based on the rates from the Gutenberg-Richter distributions in Figure 1b and on the Swiss ground motion prediction equations by *Faeh et al.* [2011]. Three-dimensional event locations from two perspectives, i.e., (d) subparallel and (e) normal to the main extent of the seismicity cloud. Circles correspond to source areas assuming a stress drop of 3 MPa [*Kanamori and Anderson*, 1975].

volume and that even a small pore fluid perturbation may be sufficient to trigger rupture that extends far beyond the pressurized zone. In this case, M_{max} could reach the value used for tectonic seismic hazard assessments (e.g., M_w7.2 for Switzerland [*Wiemer et al.*, 2009]). The Gutenberg-Richter distribution would then still relate a small but finite chance of magnitudes up to M_{max}, even if injection volumes are small [*Gischig and Wiemer*, 2013]. So the question of the actual worst case physical limit to injection-induced seismic moment release remains unresolved.

Constraints on M_{max} can be gained from physical earthquake source models that consider rate-and-state frictional behavior [*C. H. Scholz*, 1998; *Segall*, 2010] as well as hydromechanical feedbacks reproducing transient pressure fields during fluid injection. The numerical model CFRAC [*McClure*, 2012] includes these features (see supporting information for further information) and has been successfully used in the past to model induced seismicity during fluid injections [*McClure and Horne*, 2011]. In the present study, I use this model to explore how shear and normal stresses along a fault influence rupture-front propagation and to deduce if M_{max} may be well below the most conservative estimate under certain stress conditions. I consider the simplest fault configuration: a single two-dimensional fault with homogenous hydromechanical and frictional properties (Table S1). Water is injected into the middle of the fault at constant pressure (Figure 2a). A range of shear and normal stress combinations and injection pressures are applied to the fracture to

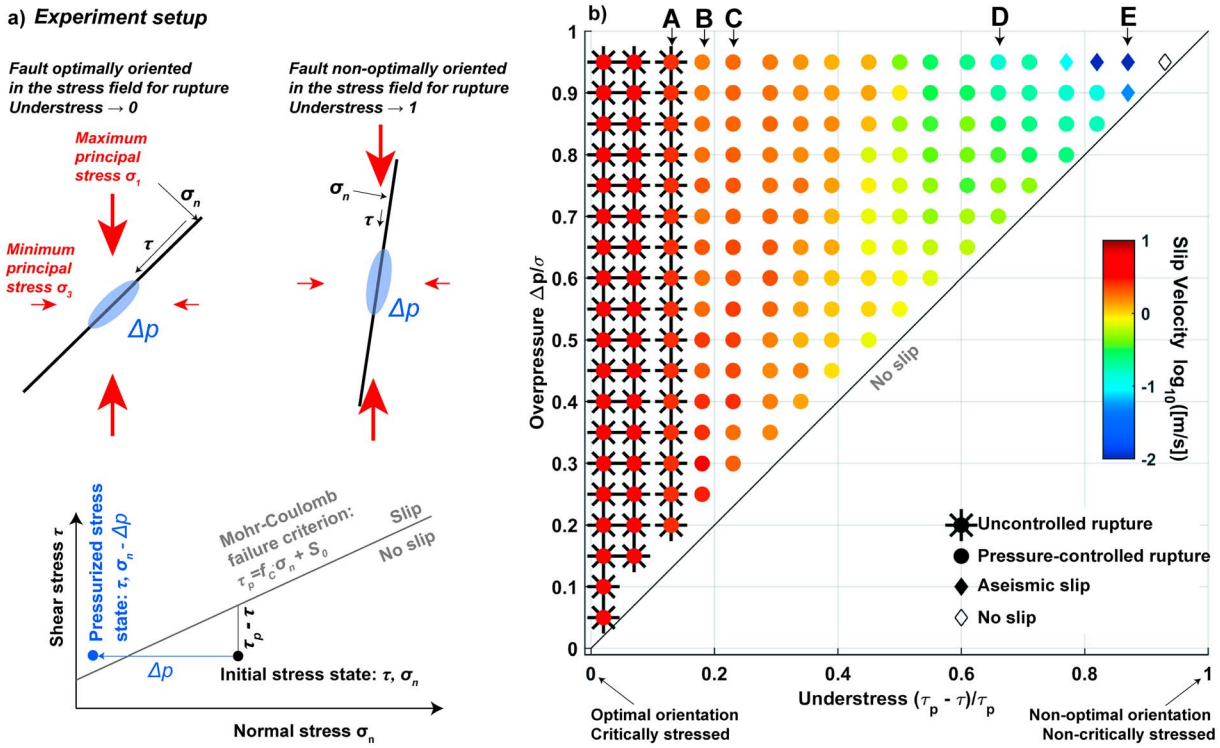

Figure 2. (a) Sketch of experiment setup. A fault with an oblique angle with respect to the principal stress directions σ_1 and σ_3 is exposed to a normal stress σ_n and a shear stress τ. The magnitude of σ_n and τ depend on the orientation of the fault. Water is injected into the fault at pressure Δp above hydrostatic. The initial stress state and the stress state during pressurization can be represented in relation to a Mohr-Coulomb failure criterion. Fault strength is defined by the friction coefficient f_c and cohesion S_0 (zero here). (b) Slip velocity and rupture propagation behavior for a suite of solutions as a function of understress (shear stress below failure limit normalized to failure stress τ_p) and overpressure (injection pressure normalized to fault normal stress). Slip velocity corresponds to the maximum value that occurred during injection (until the pressure front reached the fault tips). Cases A–E are illustrated in Figure 3.

explore the sensitivity of rupture behavior to changing fracture orientations in a constant stress field. Results demonstrate that rupture may propagate beyond the pressure front if the fault is critically stressed or arrest at the pressure front otherwise; an observation that can be used to refine induced seismic hazard analysis.

2. Scenarios for Rupture Propagation

In the first model sequence, the simulated fault is exposed to normal and shear stresses arising from in situ stress conditions at the Basel deep geothermal project at 4500 m depth [*Häring et al*., 2008] and then rotated through different orientations (details see supporting information). Consistent with the observed predominant strike-slip earthquake focal mechanisms, the intermediate principal stress σ_2 is assumed to be vertical and equal to the lithostatic weight of the overburden, and the unperturbed water pressure to be hydrostatic. The minimum principal effective stress σ'_3 is assumed to be greater than the maximum injection pressure of 30 MPa, as tensile fracture opening normal to σ'_3 was not observed during stimulation. The largest principal effective stress σ'_1 is then computed based on the assumption that the rock mass is critically stressed with a friction coefficient of 0.85.

For each fault orientation, I analyze the evolution of slip as a function of injection pressure and stress state (Figure 2b). To represent different injection pressure and stress conditions, I adapt the graphical representation of *Garagash and Germanovich* [2012]: combinations of shear stress, normal stress, and injection pressure are represented by plotting *understress* on the *x* axis (defined as $(\tau_P - \tau)/\tau_P$, where τ is initial shear stress on the fault and τ_P is the shear stress at which slip initiates based on the Mohr-Coulomb failure criterion, i.e., $\tau_P = f_C \cdot \sigma_n$, with a friction coefficient $f_C = 0.85$) and *overpressure* on the *y* axis (defined as $\Delta p/\sigma_n$, i.e., injection pressure Δp normalized by the fault effective normal stress σ_n). As understress approaches 0, the fault becomes critically stressed, i.e., it is on the verge of rupture, while understress = 1 means there is no shear stress on the fault. Note that understress and hence criticality is defined using a Mohr-Coulomb failure

criterion despite using rate-and-state friction for slip computation, because the latter is not a failure criterion and understress and criticality cannot be represented in a simple way. Injection pressures tested here correspond to overpressures of 0.05–0.95, i.e., 5–95% of the fracture effective normal stress. Understress values ranging from 0.05 to 0.95 may correspond to different fracture orientations in the Basel-type stress field ranging from optimally oriented to normal to σ_3 (Figure 2). Generally, different understress states may not only result from different fracture orientations; an optimally oriented fracture may be noncritically stressed due to recent slip and stress release. The diagonal in Figure 2b represents the frictional failure limit assuming a friction coefficient $f_C = 0.85$ and no cohesion. When $\Delta p/\sigma_n < (\tau_P - \tau)/\tau_P$ (states below the diagonal), shear stress or injection pressure is too low for slip to be induced (slip velocity $<10^{-8}$ m/s), i.e., predictions of slip initiations by rate-and-state computations are in agreement with the Mohr-Coulomb failure criterion. In contrast, if shear stress and/or injection pressures are sufficiently high (above the diagonal), slip is initiated. I observed that as injection at constant pressure continues, various styles of rupture evolution emerge as a function of stress conditions and overpressure. Symbols in Figure 2b distinguish different categories of rupture behavior: (1) uncontrolled rupture-front propagation, (2) pressure-controlled rupture-front propagation, and (3) aseismic slip. The symbols are colored according to the maximum slip velocity reached during the injection period. I always pressurize the fault until the pressure front reaches the end of the 600 m long fault to ensure that results do not depend on the extent of the pressure field.

Figure 3 shows examples of the different rupture propagation categories (Cases A–E at overpressure 0.95 in Figure 2b). In Case A, slip is induced within a small pressurized region, and, once it has initiated, the rupture-front runs out to the edges of the fault without requiring further expansion of the pressure field. The slip velocity is high (>1 m/s), and within seconds the entire fault has ruptured. This case represents an uncontrolled rupture propagation event: once rupture is triggered by pressurizing only a small fault area, it requires no further forcing to propagate to the ends of the preexisting fault. However, it does require the fault to be critically stressed (i.e., low understress). In nature, the maximum source area and slip distance—and hence the magnitude—are controlled by geologic conditions, i.e., by finite dimensions of the fault, local changes in orientation along a nonplanar fault, and/or stress field heterogeneities.

If stress conditions are less critical, the rupture propagation behavior changes. Once slip initiates, the rupture-front here again runs out quickly, but instead of propagating to the end of the fault, it arrests at or a little beyond the pressurized front (Case C). The ruptured fault area always keeps pace with the propagating pressure front. Hence, rupture-front propagation is pressure controlled. For larger rupture propagation, and thus larger seismic events, longer pressurization is required. Case B can be considered transitional—the rupture-front still propagates considerably beyond the pressure front, but not to the end of the fault.

Slip velocity in Figure 2b decreases systematically with decreasing shear stress on the fault. It is well known that substantial fault slip can occur without detectable seismic energy release when slip velocity is low [*Evans*, 1998; *Marone and Scholz*, 1988; *C. H. Scholz*, 1998]. The threshold slip velocity V_{dyn} [*Rubin and Ampuero*, 2005], below which slip is aseismic, depends on the rock mass stiffness [*C. H. Scholz*, 1998]. In Figure 2b, I defined the transition from seismic to aseismic slip to occur at $V_{\mathrm{dyn}} = 0.1$ m/s [*McClure and Horne*, 2011; *Rubin and Ampuero*, 2005]. Maximum slip velocities at high understress reach values of only 10^{-5}–10^{-4} m/s (Case E). In Cases D and E changes in both slip and rupture velocities do not occur abruptly but remain constant for long time periods and change smoothly. The rupture-front always coincides with the pressure front. At such high understress levels, there is a transition from seismic to aseismic slip, the latter constituting a third rupture style.

These results show that in the case of a fault close to criticality, rupture may run out to large distances once a sufficiently large nucleation patch has formed. The overpressure magnitude merely determines the time at which uncontrolled propagation starts. Similar studies using analytic solutions of a slip-weakening friction model also showed that for fixed frictional properties of the fault, different rupture-front propagation regimes may exist during fault pressurization depending on shear stress level [*Garagash and Germanovich*, 2012]. These studies also showed that the degree of criticality determines whether rupture runs out beyond the pressure front, while overpressure plays a secondary role. Note that rate-and-state parameters—although realistic based on laboratory- and fault-scale observations [*C. H. Scholz*, 2002]—were chosen such that uncontrolled rupture is promoted (see supporting information). Conditions that are less velocity weakening and with weakening occurring over larger slip distances would result in a transition between uncontrolled and

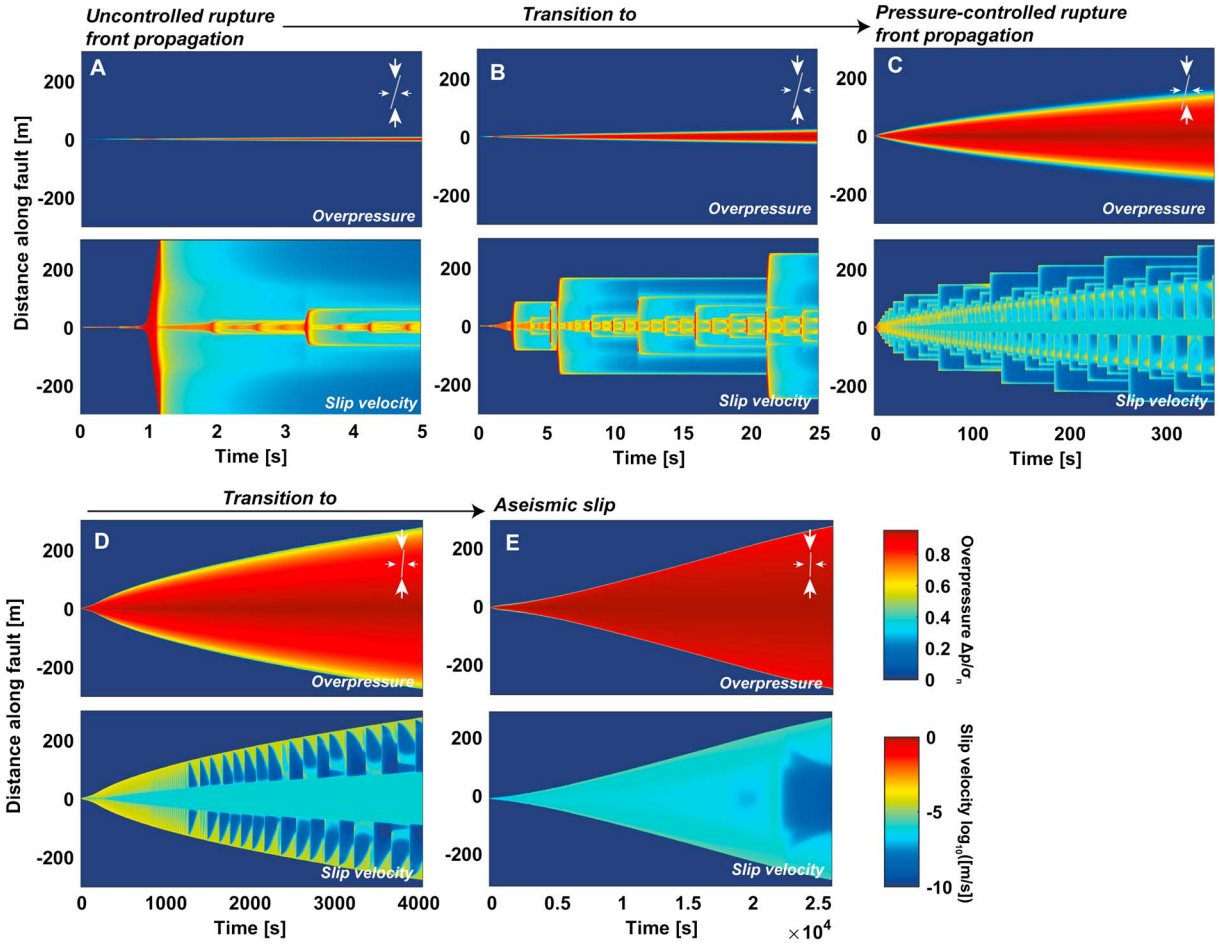

Figure 3. Examples of different rupture behavior. Cases A–E correspond to indicated solutions in Figure 2b. (top) overpressure; (bottom) slip velocity as a function of time and distance along the fault. Cases A, C, and E are typical for rupture propagation regimes classified in Figure 2b; cases B and D can be interpreted as transitional between these behaviors. The transition between seismic and aseismic rupture is defined by a threshold slip velocity of 0.1 m/s.

pressure-controlled propagation closer toward critically stressed situations (shifted to the left in Figure 2b). A comprehensive parameter sensitvitiy analysis exploring the complex rate-and-state parameter space goes beyond the scope of this study but has to be performed in future research.

3. Implications for Induced Seismic Hazard

The observation of different rupture behavior has important implications for seismic hazard assessment during reservoir stimulation. In conditions favoring uncontrolled rupture-front propagation, so-called runaway events may occur. I emphasize that the runaway events in my model represent a worst case, because the fault is assumed to be perfectly planar and to have homogeneous properties—a situation rarely if ever encountered in nature. In reality, various geological conditions—e.g., limited fault persistence, step over between fault segments, large-scale fault waviness, and stress heterogeneities—will limit the extent of rupture [*Fang and Dunham*, 2013]. It is the combined effect of these conditions, which themselves usually follow power law distributions, that is reflected in the power law magnitude distributions of both tectonic and induced earthquakes [*Ben-Zion*, 2008; *Fang and Dunham*, 2013]. If a fault zone is critically stressed, and hence in the uncontrolled propagation regime, there is little reason to believe that the dimension of the perturbed reservoir volume limits rupture propagation and that the Gutenberg-Richter distribution is truncated at magnitudes lower than the tectonic M_{max}. Such faults are sometimes known to be active from observed tectonic seismicity depending on the extent of regional seismic monitoring. This interpretation agrees with *M. D. Zoback* [2012], who warned that injection into or near active faults may result in undesired

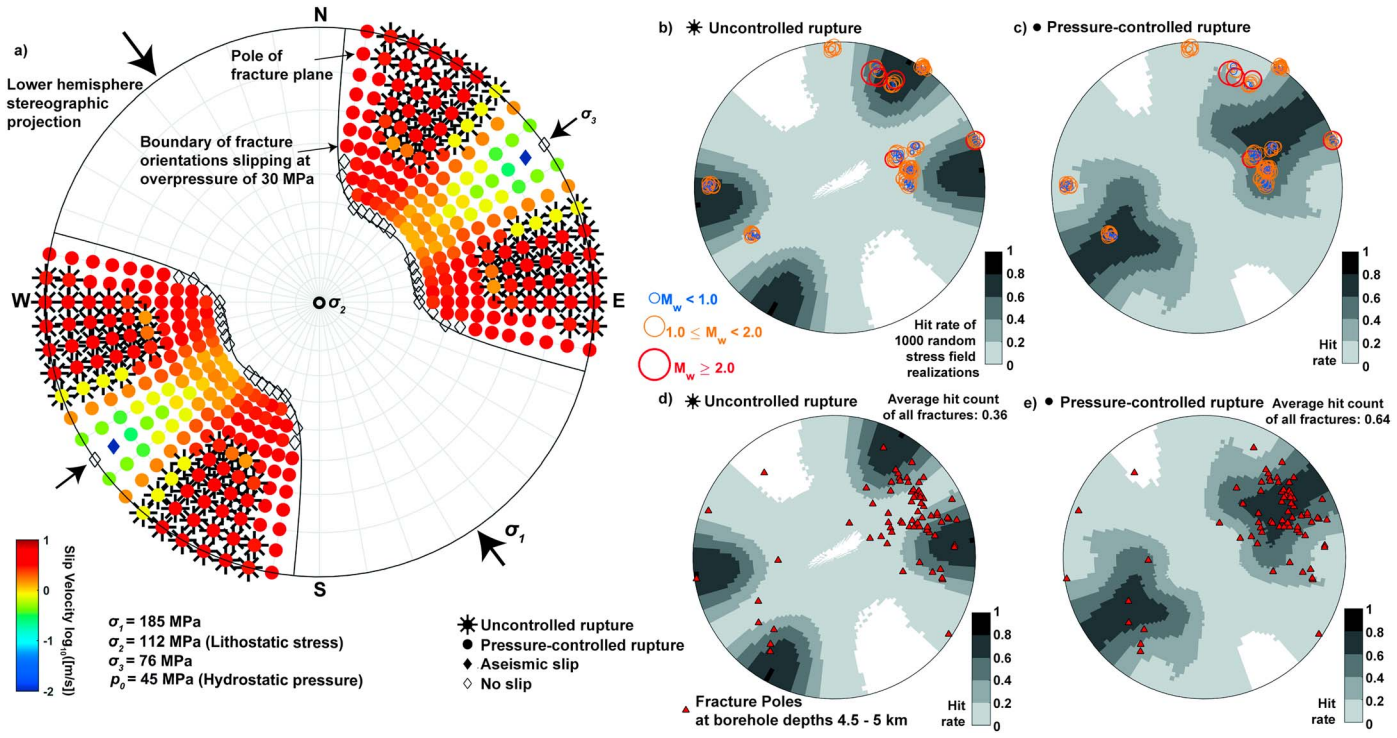

Figure 4. Rupture propagation regimes as a function of fault orientation represented in stereographic projection [*M. D. Zoback*, 2007]. Symbols represent fault poles. (a) Propagation regimes in a Basel-type stress field (4500 m depth); injection pressure = 30 MPa, the maximum value in Basel. All rupture propagation regimes described in Figure 3 are found depending on assumed fault orientation. (b–e) Hit count for different propagation regimes from a randomly perturbed Basel-type stress field (1000 realizations). Figures 4b and 4c show superimposed source orientations of induced earthquakes [*Deichmann et al.*, 2014] (Figure 1). Figures 4d and 4e show superimposed fracture orientations derived from borehole imagery between 4600 and 5000 m depth [*Ziegler et al.*, 2015].

levels of seismicity. However, if a fault zone is not critically stressed, pressure-controlled rupture propagation will result. Aforementioned geological and structural conditions will still tend to produce a Gutenberg-Richter magnitude distribution. Because rupture in this case is limited by the disturbed reservoir volume, the maximum possible moment release is closer to estimates from injection volume [*McGarr*, 2014] or perturbed reservoir volume [*Baisch et al.*, 2009], and the power law distribution may be truncated at relatively low magnitudes.

4. Source Orientations in the Basel Reservoir

A rock volume that contains faults with varying orientations can exhibit different rupture-front propagation regimes concurrently, even under the assumption of a constant stress field (Figure 2a). In addition, slip velocity also depends on fault orientation [*M. D. Zoback et al.*, 2012]. Using the stress field of the Basel EGS experiment (Figure 4), I systematically explore the dependence of rupture behavior on fault orientation (Figure 4a). For this, I determined the rupture propagation regime for all fault orientations that could be reactivated by an overpressure of 30 MPa, which corresponds to the maximum injection pressure in 2006 [*Häring et al.*, 2008]. Depending on orientation, different rupture behavior is anticipated: optimally oriented faults rupture in an uncontrolled manner, whereas along misoriented faults rupture is limited or slip is aseismic (Figure 4a).

I also account for variability in the assumed stress field. The actual stress state is uncertain, as it is difficult to measure precisely. Additionally, it can exhibit substantial spatial heterogeneity in orientation [*Valley and Evans*, 2009] and likely also in magnitude. To account for this, I computed the rupture propagation regime not only for all possible fault orientations but also for a range of randomly varied (but still spatially homogeneous) stress fields. I selected random values for the magnitudes of the three principal stress components from normal distributions, with the means indicated in Figure 4a and a 10% standard deviation. Similarly, random stress orientations were drawn from normal distributions with 10° standard deviation. Repeating this

procedure 1000 times, I tracked how frequently a certain rupture propagation regime occurred for each orientation. Stereo plots shown in Figures 4b and 4c show, for each rupture propagation regime, the "hit rate" for these 1000 random variations of the stress field. They indicate how likely a fault with given orientation will exhibit a particular rupture behavior.

Superimposed on these stereoplots are fault orientations derived for earthquakes induced during the 2006 injection. These orientations were inferred for a subset of recorded events that could be grouped into clusters with similar waveforms [*Deichmann et al*., 2014] (Figures 1a, 1d, and 1e). Focal mechanisms and relative hypocenter locations within each cluster were then combined to determine reliable fault orientations. The orientation of clusters containing the largest events ($M_w \geq 2.0$) is located close to orientations for which a high chance of uncontrolled rupture propagation is predicted (Figure 4b). In contrast, cluster orientations for smaller events ($M_w < 2.0$) coincide with orientations for which pressure-controlled rupture propagation is predicted (Figure 4c). This is not to say that largest events in Basel must be characterized as uncontrolled rupture events: we know neither the precise location of the pressure front at the time of events nor the actual source area of these events relative to the pressurized volume. Nevertheless, the largest event occurred at the periphery of the seismicity cloud (Figures 1d and 1e) and has an orientation that differs from the overall orientation of the hypocenter cloud. Possibly, it lies along a fault segment that is more critically stressed than the other faults and oriented such that larger ruptures are more likely. My models predict larger rupture propagation distances for these orientations. On the other hand, many of the smaller events occurred along faults less favorably oriented in the stress field. My models predict rupture propagation limited by the pressurized volume for these orientations. I propose that late in the injection, the pressure front encountered a preexisting structure with near-optimal orientation, resulting in more pronounced rupture propagation and larger magnitudes. This agrees with observations by *Terakawa et al*. [2012], who concluded that many smaller events occurred along nonoptimally oriented faults and required larger pressure to be induced, while larger events occurred along optimally oriented faults.

In Figures 4d and 4e, I superimpose fracture orientations derived from borehole imaging in the open-hole section (4600 and 5000 m depth) in the injection well at the Basel EGS site [*Ziegler et al*., 2015]. More of these preexisting structures fall into the pressure-controlled regime rather than the uncontrolled rupture regime, but there is also good chance for rupture along a fault oriented for uncontrolled propagation. For all these fractures, I then compute a relative rate of falling into one or the other regime: the uncontrolled—propagation regime has an average hit rate of 0.36, while the pressure-controlled regime has a hit rate of 0.64.

This analysis illustrates a method of including information on structural reservoir properties, stress field data, and source physical modeling into seismic hazard assessment prior to reservoir stimulation. Assumptions of $M_{\max}$ in induced seismic hazard analyses have been heuristic to date: $M_{\max}$ (1) is limited by reservoir size [*Baisch et al*., 2009] or injection volume [*McGarr*, 2014], (2) corresponds to the maximum possible magnitude earthquake for tectonic events [*Gischig and Wiemer*, 2013; *Wiemer et al*., 2009], or (3) is represented as a weighted average of the different options using a logic tree approach. *Mignan et al*. [2015], for instance, arbitrarily gave all options equal weight. Based on the above procedure, we may now assign weights based on our knowledge of structural reservoir properties: we can assign a weight of 0.36 to the larger and more conservative $M_{\max}$ (uncontrolled propagation) and 0.64 to the smaller reservoir-scale $M_{\max}$ (pressure-controlled propagation), instead of equal weights. A hazard curve using these weights is shown in Figure 1c. I acknowledge that computing these weights would require considering not only the variability of the stress field but also uncertainty in the structural analysis and the range of possible model parameters. As mentioned earlier, rate-and-state parameters were chosen to favor uncontrolled propagation. Thus, including a wider range of rate-and-state parameters is likely to result in a lower weight for more conservative $M_{\max}$.

5. Conclusions

This study addresses the question of whether the largest possible induced fault rupture can propagate beyond the stimulated rock mass volume. The answer is that it depends—apart from fault properties—on the orientation of natural faults and the stress field: optimally oriented faults can rupture beyond the pressurized volume and arrest where geological conditions change (i.e., breaks in fault persistence or changes in fault properties and stress conditions). Along nonoptimally oriented faults, rupture arrests within or only little beyond the pressurized front. Although it is difficult to distinguish between the two rupture propagation

regimes in data sets of observed induced seismicity, they are conceptually in agreement with observed relationships between magnitudes and fault orientation. Not only in the Basel reservoir but also in different cases in shale gas operations, it was observed that magnitudes of induced earthquakes depend on fault orientation. During hydraulic fracturing in shale gas field often only very small seismic events ($M < -1.0$) are induced. However, many cases have recently been reported in literature, in which magnitude levels suddenly rose and felt events occurred [*BC Oil and Gas Commission*, 2012; *de Pater and Baisch*, 2011; *Holland*, 2011; *Skoumal et al*., 2015; *Wolhart et al*., 2006]. In some cases, the change in seismicity levels was observed to be associated with a change of direction, in which the seismicity clouds propagated. During hydraulic fracturing near Blackpool, UK, an event sequence with magnitudes up to M_L2.3 occurred in 2011 [*Huw et al*., 2014]. Retrospectively, these events could be associated with a previously undetected fault zone optimally oriented in the stress field.

Estimating the in situ stress field and collecting structural data from the rock mass targeted for stimulation is essential in assessing and reducing induced seismic hazard. During different planning phases of a reservoir stimulation project, different levels of information on the structures (e.g., from seismic imaging, local microseismic monitoring, and borehole fracture imaging) and stress conditions (e.g., from focal mechanism analysis, and borehole stress observations) are available. At each phase, M_{max} can be constrained based on the stress field and fault information available, as well as on source physical modeling, and seismic risk estimates can progressively be refined.

Acknowledgments

The author thanks M.W. McClure for providing the CFRAC code used in this study and for reviewing the manuscript. Martin Ziegler is thanked for providing fracture orientations from the Basel borehole. I also thank Nicholas Deichmann, Jeffrey R. Moore and Joseph Doetsch for editing the manuscript and providing useful comments. Jean-Paul Ampuero and Gail Atkinson are thanked for their thorough review of the paper. Model results used to generate Figures 2–4 can be obtained from the author (gischig@erdw.ethz.ch). Earthquake source orientations in Figures 4b and 4c, as well as fracture orientation in Figures 4d and 4e, are available from cited references.

The Editor thanks Jean-Paul Ampuero and Gail Atkinson for their assistance in evaluating this paper.

References

Atkinson, G. M., H. Ghofrani, and K. Assatourians (2015), Impact of induced seismicity on the evaluation of seismic hazard: Some preliminary considerations, *Seismol. Res. Lett.*, *86*(3), 1009–1021.

Bachmann, C., S. Wiemer, J. Woessner, and S. Hainzl (2011), Statistical analysis of the induced Basel 2006 earthquake sequence: Introducing a probability-based monitoring approach for Enhanced Geothermal Systems, *Geophys. J. Int.*, *186*(2), 793–807, doi:10.1111/j.1365-246X.2011.05068.x.

Baisch, S., et al. (2009), Deep heat mining Basel: Seismic risk analysis, SERIANEX, Tech. Rep., study prepared for the Department für Wirtschaft, Soziales und Umwelt des Kantons Basel-Stadt, Amt für Umwelt und Energie.

BC Oil and Gas Commission (2012), Investigation of observed seismicity in the Horn River Basin, Tech. Rep., 29 pp., BC Oil and Gas Commission, Victoria, B. C., Canada.

Ben-Zion, Y. (2008), Collective behavior of earthquakes and faults: Continuum-discrete transitions, progressive evolutionary changes, and different dynamic regimes, *Rev. Geophys.*, *46*, RG4006, doi:10.1029/2008RG000260.

Bourne, S. J., S. J. Oates, J. J. Bommer, B. Dost, J. van Elk, and D. Doornhof (2015), A Monte Carlo method for probabilistic hazard assessment of induced seismicity due to conventional natural gas production, *Bull. Seismol. Soc. Am.*, *105*(3), 1721–1738.

de Pater, C. J., and S. Baisch (2011), Geomechanical study of Bowland Shale seismicity: Cuadrilla Resources Ltd, Synthesis Rep., 71 pp.

Deichmann, N., T. Kraft, and K. F. Evans (2014), Identification of faults activated during the stimulation of the Basel geothermal project from cluster analysis and focal mechanisms of the larger magnitude events, *Geothermics*, *52*, 84–97.

Ellsworth, W. L. (2013), Injection-induced earthquakes, *Science*, *341*, doi:10.1126/science.1225942.

Evans, K. F. (1998), Does significant aseismic slip occur on fractures in HDR systems under stimulation conditions, paper presented at 4th Int. HDR Forum Strasbourg September 28–30th, 1998.

Faeh, D., et al. (2011), ECOS-09 earthquake catalogue of Switzerland release 2011, Report and Database *Rep*., Report SED/RISK, Swiss Seismological Service ETH, Zürich.

Fang, Z., and E. M. Dunham (2013), Additional shear resistance from fault roughness and stress levels on geometrically complex faults, *J. Geophys. Res. Solid Earth*, *118*, 3642–3654, doi:10.1002/jgrb.50262.

Garagash, D. I., and L. N. Germanovich (2012), Nucleation and arrest of dynamic slip on a pressurized fault, *J. Geophys. Res.*, *117*, B10310, doi:10.1029/2012JB009209.

Giardini, D. (2009), Geothermal quake risks must be faced, *Nature*, *462*(7275), 848–849.

Gischig, V. S., and S. Wiemer (2013), A stochastic model for induced seismicity based on non-linear pressure diffusion and irreversible permeability enhancement, *Geophys. J. Int.*, *194*(2), 1229–1249.

Häring, M. O., U. Schanz, F. Ladner, and B. C. Dyer (2008), Characterisation of the Basel 1 enhanced geothermal system, *Geothermics*, *37*, 469–495.

Holland, A. (2011), Examination of possibly induced seismicity from hydraulic fracturing in the Eola Field, Garvin County, Oklahoma (Tech. Rep.) *Rep*.

Huw, C., L. Eisner, P. Styles, and P. Turner (2014), Felt seismicity associated with shale gas hydraulic fracturing: The first documented example in Europe, *Geophys. Res. Lett.*, *41*, 8308–8314, doi:10.1002/2014GL062047.

Kanamori, H., and D. L. Anderson (1975), Theoretical basis of some empirical relations in seismology, *Bull. Seismol. Soc. Am.*, *65*, 1073–1095.

Keranen, K. M., H. M. Savage, G. A. Abers, and E. S. Cochran (2013), Potentially induced earthquakes in Oklahoma, USA: Links between wastewater injection and the 2011 M_w 5.7 earthquake sequence, *Geology*, *41*(6), 699–702.

Kraft, T., and N. Deichmann (2014), High-precision relocation and focal mechanism of the injection-induced seismicity at the Basel EGS, *Geothermics*, *52*, 59–73.

Marone, C., and C. H. Scholz (1988), The depth of seismic faulting and the upper transition from stable to unstable slip regimes, *Geophys. Res. Lett.*, *15*, 621–624, doi:10.1029/GL015i006p00621.

McClure, M. W. (2012), *Modeling and Characterization of Hydraulic Stimulation and Induced Seismicity in Geothermal and Shale Gas Reservoirs*, Stanford Univ., Stanford, Calif.

McClure, M. W., and R. Horne (2011), Investigation of injection-induced seismicity using a coupled fluid flow and rate/state friction model, *Geophysics*, *76*(6), 181–198.

McGarr, A. (1976), Seismic moments and volume changes, *J. Geophys. Res.*, *81*(8), 1487–1494, doi:10.1029/JB081i008p01487.
McGarr, A. (2014), Maximum magnitude earthquakes induced by fluid injection, *J. Geophys. Res. Solid Earth*, *119*, 1008–1019.
Mena, B., S. Wiemer, and C. Bachmann (2013), Building robust model to forecast the induced seismicity related to geothermal reservoir enhancements, *Bull. Seimsol. Soc. Am.*, *103*(1), 383–393.
Mignan, A., D. Landtwing, P. Kästli, B. Mena, and S. Wiemer (2015), Induced seismicity risk analysis of the 2006 Basel, Switzerland, Enhanced Geothermal System project: Influence of uncertainties on risk mitigation, *Geothermics*, *53*, 133–146.
Petersen, M., et al. (2008), Documentation for the 2008 update of the United States National Seismic Hazard Maps, *U.S. Geol. Surv. Open File Rep., 2008-1128*, p. 61.
Rubin, A. M., and J.-P. Ampuero (2005), Earthquake nucleation on (aging) rate and state faults, *J. Geophys. Res.*, *110*, B11312, doi:10.1029/2005JB003686.
Scholz, C. H. (1998), Earthquakes and friction laws, *Nature*, *391*, 37–42.
Scholz, C. H. (2002), *The Mechanics of Earthquakes and Faulting*, 439 pp., Cambridge Univ. Press, Cambridge, U. K.
Segall, P. (2010), *Earthquake and Volcano Deformation*, Princeton Univ. Press, Princeton, N. J.
Skoumal, R. J., M. R. Brudzinski, and B. S. Currie (2015), Earthquakes induced by hydraulic fracturing in Poland Township, Ohio, *Bull. Seismol. Soc. Am.*, *105*(1), 189–197.
Terakawa, T., S. A. Miller, and N. Deichmann (2012), High fluid pressure and triggered earthquakes in the enhanced geothermal system in Basel, Switzerland, *J. Geophys. Res.*, *117*, B07305, doi:10.1029/2011JB008980.
Valley, B., and K. F. Evans (2009), Stress orientation to 5 km depth in the basement below Basel (Switzerland) from borehole failure analysis, *Swiss J. Geosci.*, *102*, 467–480.
Wiemer, S., D. Giardini, D. Faeh, N. Deichmann, and S. Sellami (2009), Probabilistic seismic hazard assessment of Switzerland: Best estimates and uncertainties, *J. Seismol.*, *13*(4), 449–478.
Wolhart, S. L., T. A. Harting, J. E. Dahlem, T. Young, M. J. Mayerhofer, and E. P. Lolon (2006), Hydraulic fracture diagnostics used to optimize development in the Jonah field, paper presented at SPE Annual Technical Conference and Exhibition. Society of Petroleum Engineers.
Ziegler, M., B. Valley, and K. F. Evans (2015), Characterisation of natural fractures and fracture zones of the Basel EGS reservoir inferred from geophysical logging of the Basel-1 well, paper presented at World Geothermal Congress Melbourne, Australia, 19–25 April.
Zoback, M. D. (2007), *Reservoir Geomechanics*, 449 pp., Cambridge Univ. Press, New York.
Zoback, M. D. (2012), Managing the seismic risk posed by wastewater disposal, *Earth Mag.*, 38–43.
Zoback, M. D., A. Kohli, I. Das, and M. McClure (2012), The importance of slow slip on faults during hydraulic fracturing stimulation of shale gas reservoirs, paper presented at SPE Americas Unconventional Resources Conference, Pittsburgh, Pa.